RSC Advances

PAPER

View Article Online
View Journal | View Issue

Cite this: *RSC Adv.*, 2025, **15**, 17466

Solid-state lithium-ion battery employing $LiBH_4$–ZrO_2 as a solid-state electrolyte†

Asya Mazzucco,[a] Robert J. Wolterbeek,[b] Valerio Gulino,[bc] Mauro F. Sgroi,[a] Peter Ngene,[b] Petra E. de Jongh[b] and Marcello Baricco*[a]

Received 7th February 2025
Accepted 19th May 2025

DOI: 10.1039/d5ra00916b

rsc.li/rsc-advances

$LiBH_4$ has been extensively investigated as a solid-state electrolyte for Li-ion battery applications. The crucial point is that the operating temperature for this material needs to be above 120 °C, due to its low ionic conductivity at room temperature. In this study, the Li-ion conductivity of $LiBH_4$ has been enhanced by mixing it with ZrO_2. The optimal composition of the mixture was found to be 37 v/v% of ZrO_2, exhibiting a Li-ion conductivity of 3.32×10^{-4} S cm^{-1} at 60 °C. The electrochemical stability window of the mixture (2.4 V *vs.* Li^+/Li) is slightly higher compared to that of pure $LiBH_4$. The optimized mixture was used as an electrolyte in TiS_2/Li all-solid-state Li-ion batteries. Two batteries were successfully cycled at 60 °C. The effect of charging profile was investigated to improve the performance of the battery.

Introduction

Lithium-ion batteries find several applications in different sectors, from compact portable electronic devices to electric vehicles. Nevertheless, conventional liquid electrolytes used nowadays in Li-ion batteries raise concerns from a safety point of view, because of possible leakages, leading to the loss of the electrolyte.[1,2] Due to the highly flammable nature of organic solvents, like tetrahydrofolate (THF), in which salts usually are dissolved,[3] conventional electrolytes are related to uncontrolled thermal runway phenomena,[4] that can lead to the explosion of the battery and to a reduced lifespan. Solid-state electrolytes (SSE) emerged as promising alternatives, due to their relatively high Li^+ transference number, robust stability across a broad temperature range, leading to solid-state batteries (SSB), with elevated energy density.[1,2,5]

Several materials have been explored as potential candidates for SSE applications in Li-ion batteries,[6] including LISICON-based,[7] lithium lanthanum titanate-based[8] and Li_2NH.[9] In recent years, complex hydrides have also gained attention as promising SSE for SSB.[10] Among complex hydrides, several good candidates have been identified, such as $LiAlH_4$,[11,12] $Li_2B_{12}H_{12}$ (ref. 13 and 14) and $LiBH_4$.[15,16] $LiBH_4$ has two possible crystalline phases: at room temperature (RT) it has an orthorhombic crystal structure, characterized by a low ionic conductivity. However, it undergoes a phase transition to a hexagonal phase at around 110 °C, reaching a superionic Li-ion conductivity (around 10^{-3} S cm^{-1}).[17] It is possible to increase the ionic conductivity of $LiBH_4$ at RT in two different ways: by performing an anionic substitution, stabilizing the high ionic conductive hexagonal phase[15,16,18,19] or by the formation of highly-conductive interlayers through the addition of porous oxides.[20] The impact of adding different types of oxides, like SiO_2, Al_2O_3, ZrO_2 and MgO, to $LiBH_4$ has been recently investigated, considering different pore filling ratios, which determine different thickness of the conductive interlayer. Mixtures showed an ionic conductivity of the order of $10^{-4}/10^{-5}$ S cm^{-1}, as reported for $LiBH_4$–SiO_2,[21,22] $LiBH_4$–Al_2O_3,[21–24] $LiBH_4$–ZrO_2 (ref. 20 and 25) and $LiBH_4$–MgO systems.[20,25]

The precise mechanism that leads to the observed enhancement of Li-ion conductivity is still under investigation. One of the proposed explanations is that the interlayer formed at the interface by the interaction of $LiBH_4$ with the oxide results in a structure characterized by fast Li-ion pathways, that facilitate Li-ion conduction.[26–28] Lambregets *et al.*[29] studied the role of interface interactions in achieving high ionic conductivity in $LiBH_4$–SiO_2 nanocomposites, focusing on how the local pore structure and surface chemistry of the oxide influence the ionic mobility of the complex hydrides. Their findings demonstrate that the crystal structure of chosen oxides significantly influences the ionic conductivity of $LiBH_4$–SiO_2 nanocomposites. A strong correlation emerged between the thickness of the silica pore walls and the fraction of $LiBH_4$ in the nanopores, with thicker pore walls leading to a proportional increase in the fraction of highly dynamic $LiBH_4$. This effect was attributed to charge distributions within the silica. In fact, the ^{29}Si NMR spectra of the nanocomposites revealed a new silicon site,

---

[a] *Department of Chemistry, Inter-departmental Center NIS and INSTM, University of Turin, Via Pietro Giuria 7, 10125 Torino, Italy*

[b] *Materials Chemistry and Catalysis, Debye Institute for Nanomaterials Science, Utrecht University, Universiteitsweg 99, 3584 CG, Utrecht, The Netherlands*

[c] *LeydenJar, Luchthavenweg 10, 5657 EB Eindhoven, The Netherlands*

† Electronic supplementary information (ESI) available. See DOI: **https://doi.org/10.1039/d5ra00916b**

resonating at $\delta(^{29}Si) \approx -25$ ppm, predominantly located at the silica/$LiBH_4$ interface, which likely plays a significant role in enhancing ionic conduction. The interaction between $LiBH_4$ and the oxide has been carefully investigated and the formation of silicon-hydride–borohydride and silicon-oxide–lithium bonds at the interface between $LiBH_4$ and SiO_2 has been observed.[29] The study of the Li-ion conductivity in the $LiBH_4$–SiO_2 system performed by Lambregets *et al.*[30] suggested the presence of two different configurations of $LiBH_4$ in relation to the added silica. One is a dynamic and amorphous fraction near the SiO_2 pore walls, which allows the fast mobility of Li^+ and BH_4^- ions, while the other fraction is a less-dynamic and bulk-like fraction, situated in the core of the pores. De Kort *et al.*[31] applied X-ray Raman Scattering spectroscopy to further investigate the characteristics of the interface area between $LiBH_4$ and oxides. By confirming the formation of a nanocomposite between the ionic conductors and the metal oxides, they showed that, in the case of boron-based hydrides, like $LiBH_4$, the original tetragonal (BH_4) structure transforms predominantly into trigonal boron, resembling –BH_3, with a bond character akin to that of "B–O". The formation of this structure, in combination with a high fraction of interfaces in the composite, plays an important role in increasing the ionic conductivity. In a recent study, Nakagawa *et al.*[32] visualized, for the first time, the Li distribution in $LiBH_4$–ZrO_2 composites on the nanoscale level, by using energy-filtered TEM. By combing TEM and NMR results, they showed that the ZrO_2 particles are covered by an amorphous and nanoscale $LiBH_4$ thin films, which leads to an increase of the Li-ion conductivity. Scheiber *et al.*[33] highlighted the role of harsh conditions of ball milling in the $LiBH_4$–ZrO_2 system in increasing Li-ion conductivity, proving that μm-sized ZrO_2 particles serve as an extra grinding medium, creating ultrasmall, nm-sized, $LiBH_4$ crystallites, that leads to the formation of Li^+ pathways at the conductor/conductor grain boundaries. In addition, another effect of the increased ionic conductivity in ball-milled $LiBH_4$–ZrO_2 was attributed to the creation of heterojunctions at the interface between the conductor ($LiBH_4$) and the insulator (ZrO_2). The interfacial regions between the conductor and insulator may offer fast mobility pathways, allowing long-range ion transport, leading to a high defect-mediated ion conductivity.

Previous studies highlighted that $LiBH_4$–ZrO_2 is a promising SSE, but experimental investigations are missing for application in SSB. The aim of this study is the optimization of the composition of $LiBH_4$–ZrO_2 based composites, to be used as SSE. The impact of using different porosity structure of ZrO_2 and samples with different compositions was taken in consideration, aiming to optimize the pore filling, *i.e.* the volume of $LiBH_4$ in relation to the pore volume of ZrO_2, essential to obtain the highest possible Li-ion conductivity.[20] The electrochemical stability window, assessed through cyclic voltammetry, was used to highlight the impact of the used oxide on the electrochemical stability of $LiBH_4$. A SSB was obtained using a TiS_2-|SSE|Li configuration, and it was cycled at 60 °C, in order to assess possible applications of the $LiBH_4$–ZrO_2 composite as a SSE.

Experimental

Synthesis

The manipulation of the prepared samples was performed in an Argon-filled glovebox (MBraun Lab Star glove box supplied with pure 5.5 grade Argon, 95% from Sigma Aldrich). Pure $LiBH_4$ (purity >95% from Alfa Aesar) and pure ZrO_2 (type 1, called RC-100: Daiichi Kikenso RC-100, Gimex; type 2, called OX-201: Daiichi Kikenso DK-1, Gimex) were used as starting materials. Details on used ZrO_2 are reported in Table S1 in the ESI.† All samples were prepared by ball milling (BM) technique by using a Fritsch Pulverisette 6 planetary mill, using an 80 mL tungsten carbide vials with tungsten carbide balls (5 mm outside diameter). Before preparing all samples, the following steps were followed:

- The pure $LiBH_4$ was ball-milled for a total time of 2 h under Argon atmosphere at 480 rpm for periods of 10 min of milling, separated by 2 min breaks to avoid overheating;
- The pure ZrO_2 was pelletized with 0.5 ton, using a 2 cm pellet die, and it was dried under dynamic vacuum, by heating at 5 °C min^{-1} up to 300 °C, and holding at that temperature for 6 hours;
- The mechanochemical treatment of samples was performed for a total time of 30 min under Argon atmosphere at 300 rpm, for periods of 10 min of milling, separated by 2 min breaks to avoid overheating;
- The ball-to-sample mass ratio was 30 : 1 and approximately 1 g of mixture was prepared for each sample.

Prepared samples are reported in Table 1.

Surface area analysis

The surface properties of ZrO_2 were analyzed by N_2 adsorption at 77 K in a TriStar Plus II gas-volumetric apparatus (Micromeritics, Norcross, GA, USA). The specific surface area (S_{BET}) was calculated by fitting the experimental data points with a Brunauer–Emmett–Teller (BET) isotherm[34] and it was 99 $m^2\ g^{-1}$ for RC-100 and 74 $m^2\ g^{-1}$ for OX-201. The density of ZrO_2 used for calculation is 5.89 g cm^{-3} as reported in the literature.[35] The pore volume (V_p) was derived from the volume of absorbed nitrogen at $p/p_0 = 0.95$ and it was 0.29 $cm^3\ g^{-1}$ for RC-100 and 0.26 $cm^3\ g^{-1}$ for OX-201. The fraction of pore filled in the mixtures was obtained from the ratio of the $LiBH_4$ volume per gram of ZrO_2 to V_p. Assuming a uniform layer of $LiBH_4$ on the oxide surface, the thickness of the $LiBH_4$ layer covering the oxide was determined, and obtained values are reported in Table 1.

X-ray powder diffraction and rietveld analysis

Samples in powder form were characterized by X-ray Powder Diffraction (XRD) at RT (*ex situ*) using a Panalytical X-pert Pro MPD (Cu $K_{\alpha1} = 1.54059$ Å, $K_{\alpha2} = 1.54446$ Å) in Debye–Scherer configuration. Patterns were collected in the 2θ range from 10° to 80°, with a time step of 160 s. Glass capillaries (0.8 mm) were used as sample holders and they were filled and sealed under Ar atmosphere inside the glove box, to ensure the controlled atmosphere during the measurement. The Rietveld refinement

Table 1 Composition, fraction of pore filled and thickness of $LiBH_4$ layer of the synthetized samples

Sample	Oxide	Oxide [a](wt%)	Oxide [b](v/v %)	Fraction of pore filled [c](%)	Thickness of $LiBH_4$ [d](nm)
RC 1	RC-100	72.1	23	200	5.9
RC 2	RC-100	86.6	42	80	2.3
RC 3	RC-100	94.5	66	30	0.9
RC 4	RC-100	63.3	16	300	8.8
RC 5	RC-100	83.8	37	100	2.9
RC 6	RC-100	87.8	45	72	2.1
OX 1	OX-201	74.7	25	196	6.9
OX 2	OX-201	94.3	65	35	1.2
OX 3	OX-201	89.8	50	66	2.3

[a] wt% is referring to the percentage of oxides in weight inside the prepared sample (*e.g.* to prepare 1 g batch for sample **RC 1**, 0.721 g of oxides and 0.279 g of $LiBH_4$ were used). [b] v/v% is referring to the percentage of oxides in volume inside to the total volume of the synthesised sample. [c] The calculation of the fraction of pore filled was performed by dividing the volume occupied by $LiBH_4$ amount which is present per each gram of ZrO_2 by the pore volume (V_p). [d] The calculation of the thickness of $LiBH_4$ was based on the BET surface area of the oxides, assuming a flat geometry.

of XRD patterns was conducted utilizing the Materials Analysis Using Diffraction (MAUD) software.[36] The COD (Crystallography Open Database) codes for the various crystal phases corresponding to the files used for the Rietveld refinement are indicated in the text.

Attenuated total reflection infrared spectroscopy

Infrared spectra were collected by Attenuated Total Reflection Infrared Spectroscopy (IR-ATR) using a Bruker Alpha-P spectrometer, equipped with a diamond crystal. The instrument is located inside a nitrogen-filled glovebox. All spectra were recorded with a resolution of 2 cm^{-1} in a 3000–500 cm^{-1} range, with an average number of scans of 50.

Electrochemical impedance spectroscopy

By using a Specac Mini Pellet hydraulic press (250 MPa), the mixtures were pelletized, with a diameter of 10 mm and an amount of sample equivalent to a theoretical volume between 30 and 33 mm^3. The Electrochemical Impedance Spectroscopy (EIS) measurements were performed using an AMETEK PARSTAT MC potentiostat/galvanostat and a custom-made sample cell (Fig. 1) in the temperature range of RT < T < 140 °C, collecting data every 10 °C. The impedance data were analyzed using VERSASTUDIO and DECIM,[37] a custom-made software designed by H.P. Rodenburg from Utrecht University.

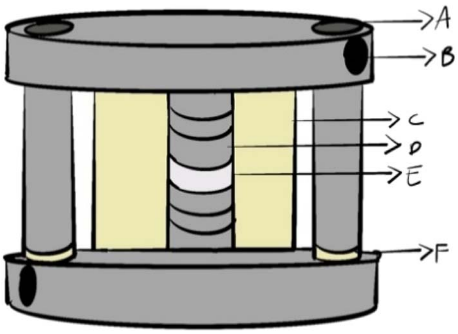

Fig. 1 Custom made cell scheme. (A) screw, (B) banana plug input, (C) sample holder in PEEK, (D) current collectors with two O-rings to avoid air leak, (E) sample, (F) PEEK attached to the screw to avoid shortcircuit.

Cyclic voltammetry

Cyclic voltammetry (CV) was applied to assess the oxidative limit of the electrochemical stability window. The $LiBH_4$–ZrO_2 composite was blended for 5 minutes in agate mortar with Ketjenblack EC600JD carbon black (CB), obtained from Akzo Nobel Chemicals, in a weight ratio of 1 : 1. The SSE was transferred inside the custom-made cell and pressed at 125 MPa with a hydraulic press. Then the SSE + CB mixture was added to cover the SSE pellet and the whole system was compressed under a working pressure of 250 MPa. As the last assembly step, a lithium disk (thickness 0.38 mm, 99.9% trace metal base from Sigma-Aldrich) was added as counter and reference electrode. The cells underwent testing using a potentiostat/galvanostat AMETEK PARSTAT MC at RT. CV measurements were conducted within a voltage range of 1.0 V to 5 V *versus* Li^+/Li at a scanning rate of 100 μV s^{-1}.

Battery assembly

The assembly process follows the same step of the CV cell, but replacing the CB with TiS_2, which was chosen as the active material for the cathode. The TiS_2 and the selected SSE sample powders were blended in a 40 : 60 weight ratio. The resulting mixture was employed as the positive electrode. Two different approaches were followed for battery cycling. The first battery was charged under a classic continuous charge (CC) profile, operating with a current density of 23.9 mA g^{-1} (C/10). The second battery was charged following a pulsed charge (PC) profile, using 5 second charge and 0.5 second discharge steps, operating at the same current density of 23.9 mA g^{-1} (C/10). The applied voltage range for the galvanostatic cycling was 1.5–2.5 V.

Results and discussion

Structural analysis of $LiBH_4$–ZrO_2 composites

As an example for samples obtained with different oxides, results of the XRD analysis are shown in Fig. 2 for selected

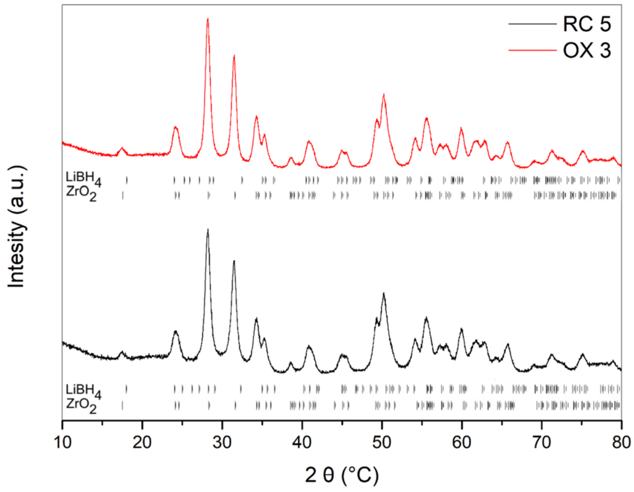

Fig. 2 XRD pattern of samples **RC 5** (bottom) and **OX 3** (top). Sticks, obtained by Rietveld refinement, show the position of diffraction peaks for both orthorhombic $LiBH_4$ (COD code 1504402) and monocline ZrO_2 (COD code 9007485) phases.

composites (**RC 5** and **OX 3C**). Results for other samples are reported in ESI (Fig. S1 and S2).† The reported patterns show mainly the diffraction peaks of the ZrO_2 phase. Some peaks correlated to the $LiBH_4$ orthorhombic phase are visible for samples with lower amounts of the oxide. Due to the high scattering power of the heavy atoms, a decrease in the relative intensity of diffraction peaks related to the $LiBH_4$ orthorhombic phase is observed by increasing the fraction of ZrO_2 in the mixture. The Rietveld refinement was performed on all the acquired XRD patterns, considering orthorhombic $LiBH_4$ (space group *Pnma*) and monoclinic ZrO_2 (space group $P2_1/c$) as crystal structures. The COD codes corresponding to the files used for the Rietveld refinement are 9007485 for ZrO_2 and 1504402 for $LiBH_4$, respectively. Table S2 in the ESI† provides the obtained weight percentage (% wt) and volume (% vol) of ZrO_2 in all the prepared samples, along with the cell parameters and cell volume for both $LiBH_4$ and ZrO_2. Cell parameters of pure starting materials are also reported for comparison.

Values of cell parameters obtained for both ZrO_2 and $LiBH_4$ phases remain rather constant and closely match those of the pure starting materials. This would suggest that no chemical interaction occurred between ZrO_2 and $LiBH_4$, during the ball milling, because there are no new crystalline compounds detected, as previously reported in the literature for other $LiBH_4$-oxide systems.[20] On the other hand, from Table S2 in the ESI,† it can be observed that results of % wt and % vol of the added oxide for all the samples, obtained from the Rietveld refinement, are different with respect to the initial nominal values, as reported in Table 1. This discrepancy can be attributed to the formation, at the interface between $LiBH_4$ and the oxide, of an amorphous layer or to a phase with a reduced long-range order, as reported by Nakagawa *et al.*,[32] which is not detectable through XRD. The difference between the nominal value of the oxide volume percentage and that obtained through the Rietveld refinement is shown in Fig. S3 in the ESI,† as a function of the oxide volume percentage derived from the Rietveld refinement. It can be seen that the addition of a higher amount of oxide to the sample results in a higher discrepancy between the initial and measured volume percentages. So, from the acquired data, it appears that a higher amount of added oxides leads to an increased formation of a new phase at the $LiBH_4$–ZrO_2 interface.

The change in the chemical nature of the samples upon ball milling was investigated by comparing results of the IR-ATR analysis of prepared composites to those obtained for pure $LiBH_4$ and ZrO_2 (Fig. S4 in the ESI†). The IR-ATR spectra of samples **RC 5** and **OX 3** are shown in Fig. 3, while those obtained for other samples are reported in the ESI (Fig. S5 and S6).† As already reported in the literature,[18,38–40] the orthorhombic $LiBH_4$ spectra show main absorption bands in two different regions, *i.e.* the 2400–2000 cm^{-1} and 1600–800 cm^{-1} ranges, which correspond, respectively, to the B–H stretching and bending vibrational modes. In the 500–760 cm^{-1} range, absorption bands related to ZrO_2 are present. The spectroscopic band related to the Zr–O bond is located around 583 cm^{-1}, while the Zr–O–Zr bond can be observed around 506 cm^{-1}, as reported in the literature.[41] The band around 670 cm^{-1} is produced by a Zr–O bending vibrations.[42] It can be concluded that the addition of ZrO_2 does not change significantly the vibrational properties of orthorhombic $LiBH_4$ and monoclinic ZrO_2, confirming the formation of a physical mixture between the two components. Structural changes developed at the interface, due to the ball milling process, cannot be highlighted by IR-ATR analysis, because of the very small volume fraction of the interlayer.

Li-ion conductivity

In order to identify the optimal composition of the SSE for the battery assembly, EIS measurements have been carried out to determine the Li-ion conductivity of prepared samples. The resistance of the SSE was determined by fitting the impedance

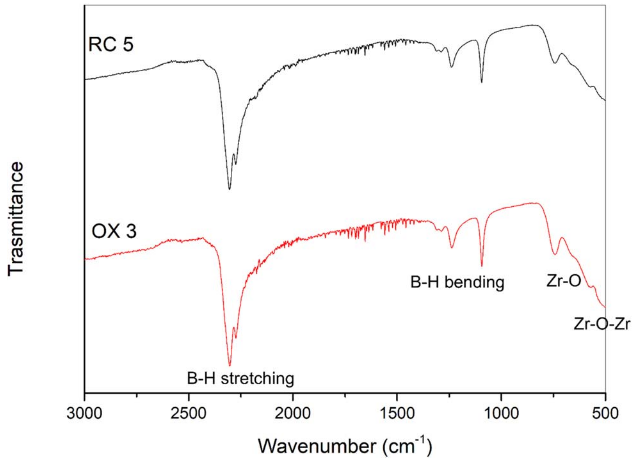

Fig. 3 IR-ATR spectra of samples **RC 5** and **OX 3**. The FTIR signals related to the B–H stretching, the B–H bending and to the vibrations of the Zr–O and of the Zr–O–Zr bonds have been evidenced.

data with an electrical circuit equal to LR(RQ)Q, as obtained from the Nyquist plots. Fig. S7 in the ESI† shows an example of the impedance spectra of **RC 5** obtained at 40 °C and 100 °C, displayed as a Nyquist plot, together with the fitting curves and lines. Data acquired from the fitting are reported in Table S3 in the ESI.† The Nyquist plot obtained, at specific temperatures, for all other samples are reported in Fig. S8 in the ESI.† Only the first heating cycle was considered, since all prepared samples showed good stability during cooling and heating ramps. As an example, 3 heating/cooling cycles for sample **OX 2** are reported in Fig. S9 of ESI.†

The Li-ion conductivity is reported, as a function of the inverse of the temperature, in Fig. 4a for samples from **RC 1** to **RC 6** and in Fig. 4b for samples from **OX 1** to **OX 3**. The result of the EIS measurement on pure $LiBH_4$ is also reported in Fig. 4a and b for comparison. The highest Li-ion conductivity at 40 °C was achieved in sample **RC 2** (1.61×10^{-4} S cm^{-1}) and sample **OX 3** (2.45×10^{-4} S cm^{-1}), which is about 4 orders of magnitude higher than that of pure $LiBH_4$.

The activation energy (E_a) for all prepared samples and pure $LiBH_4$ was calculated from the temperature (T) dependence of the Li-ion conductivity (σ) according to $\sigma = (\sigma_0/T)\cdot\exp(-E_a/kT)$, where σ_0 is a pre-exponential factor and k is the Boltzmann constant. Data have been obtained by fitting linearly the $\ln(\sigma\cdot T)$ *vs.* $1/T$ plot of the data points below 80 °C, and results are reported in Table 2. The obtained E_a values are significantly lower than those reported in the literature for pure $LiBH_4$ (0.75 ± 0.07 eV)[43] and they are comparable to those obtained for similar SSEs reported in the literature.[20,44]

The obtained values of Li-ion conductivity as a function of the pore filling are reported, for several temperatures, in Fig. 5, assuming that pores of ZrO_2 are completely filled by $LiBH_4$ during the BM synthesis. The relation between the Li-ion conductivity and the thickness of the $LiBH_4$ layer is reported in Fig. S10 in the ESI.†

Fig. 5a shows that the highest Li-ion conductivity at 40 °C for RC-type samples was achieved for sample **RC 2**, with 80% pore filling. When the temperature is increased, the highest Li-ion conductivity was achieved for sample **RC 5**, that has a 100% pore filling. Fig. 5b shows that the highest Li-ion conductivity at all temperatures for OX type mixtures was achieved for sample **OX 3**, with 66% pore filling. The need to maintain a conductive pathway for fast ion conduction is theoretically possible above 100% of pore filling. On the other hand, as reported in the literature,[20] the highest Li-ion conductivity in mixtures of $LiBH_4$ with metal oxides is achieved when a pore filling in the range of 80–100% is realized. In fact, during ball milling, original pores of the oxide can be destroyed, and new ones can be created. As an example, the highest Li-ion conductivity for $LiBH_4$–SiO_2 system (4.1×10^{-5} S cm^{-1} at 40 °C) was achieved at 80% of pore filling,[20] while, for $LiBH_4$–MgO, it was achieved at 100% of pore filling (2.86×10^{-4} S cm^{-1} at 20 °C).[25]

The improved Li-ion conductivity due to the addition of ZrO_2 can be related to the formation of a new phase at the interface, in which the ion migration path is favourite with a reduced activation energy, such as an amorphous thin layer of $LiBH_4$ around ZrO_2 particles, as reported by Nakagawa *et al.*[32] The obtained results can be also explained by considering the thickness of the $LiBH_4$ layer, as reported in Table 1 and Fig. S10.† **RC 5** contains a 2.9 nm $LiBH_4$ layer, which is considered a bulk-like fraction, as suggested by Sander *et al.*[30] This fraction does not form a highly conductive interface with the oxide, and it undergoes a phase transition to the hexagonal structure upon heating, contributing to the Li-ion conductivity at the highest temperatures. Therefore, a high ionic conductivity for sample **RC 5** above 110 °C is obtained. **RC 2** has a thickness of 2.3 nm, and thus it has a lower amount of $LiBH_4$ bulk-like, and thus a higher amount of the interface fraction which contributes to the high Li-ion conductivity at lower temperatures.

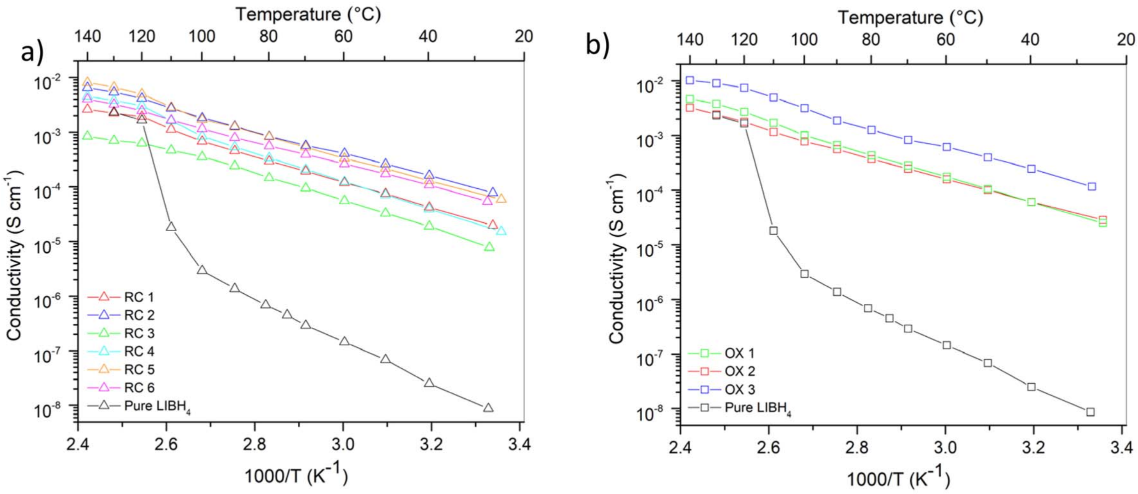

Fig. 4 Li-ion conductivity determined through a temperature-dependent EIS during the first heating ramp for samples from **RC 1** to **RC 6** (a) and from **OX 1** to **OX 3** (b). The Li-ion conductivity of pure $LiBH_4$ is reported for comparison.

Table 2 Activation energy (E_a), pre-exponential factor (σ_0) and Li-ion conductivity at 60 °C (σ) of prepared samples

Sample	**RC 1**	**RC 2**	**RC 3**	**RC 4**	**RC 5**	**RC 6**	**OX 1**	**OX 2**	**OX 3**
E_a (eV)	0.48	0.45	0.48	0.57	0.49	0.44	0.52	0.47	0.47
σ_0 (S cm^{-1})	1.92×10^6	9.16×10^5	3.90×10^5	2.13×10^7	3.60×10^6	4.13×10^5	4.70×10^6	6.76×10^5	2.38×10^6
σ (S cm^{-1}) at 60 °C	1.19×10^{-4}	4.10×10^{-4}	5.56×10^{-5}	1.24×10^{-4}	3.33×10^{-4}	2.63×10^{-4}	1.75×10^{-4}	1.57×10^{-4}	6.18×10^{-4}

Fig. S11 in ESI† reports the comparison of the Li-ion conductivity of **OX 1**, **OX 2** and **OX 3** *vs.* **RC 1**, **RC 2** and **RC 3** samples, which have a comparable thickness layer of $LiBH_4$. In all cases, the sample that was prepared using OX-201 ZrO_2 shows a higher ionic conductivity, compared to that prepared using RC-100 ZrO_2. This result can be linked to the lower S_{BET} and V_p values obtained for OX-201 with respect to RC-100. Even if samples have the same thickness of the $LiBH_4$ layer of 2.3 nm, **OX 3** possesses a higher mechanical stability than **RC 2**, due to a reduced total surface area, affecting the Li-ion conductivity positively, as already reported in the literature.[45,46]

RC 5 was preferred over **RC 2** and **OX 3** as the optimal sample for the electrochemical stability measurement, and it was selected for test as SSB. This selection was dictated by two reasons. The first one is due to the similar Li-ion conductivity of **RC 5** and **RC 2** samples at 30 °C and 60 °C, as shown in Fig. 4a. The second one is because **RC 5**, showing a pore filling of 100%, allows a comparison with existing literature data for other $LiBH_4$-oxides systems. In fact, an SSB with a $LiBH_4$–MgO composite with 100% pore filling as SSE has already been assembled, and it was able to cycle successfully at room temperature.[25] As a consequence, having **RC 2** and **OX 3** samples a pore filling of 80% and 66%, respectively, further investigations have been limited to the **RC 5** sample.

Electrochemical stability

In order to evaluate the electrochemical stability window of $LiBH_4$–ZrO_2 as SSE, CV measurements at RT were performed on **RC 5**. In Fig. 6, one cathodic (reduction) peak and one anodic (oxidation) peak have been observed during the first cycle. The current collectors of the custom-made cell are made of stainless steel AISI 304, which is prone to oxidation and reduction under measurement conditions. Peaks of corroded/oxidized stainless steel 304 have been reported in literature at 1.5 and 2 V *vs.* Li^+/Li, assigned to the reduction of the air-formed Fe-oxide and/or Cr-oxide and other pitting corrosion products.[47–49] As can be observed in Fig. 6, after performing several cycles, the contamination peaks due to stainless steel are no longer present.

The oxidative limit was determined at ~2.4 V *vs.* Li^+/Li, which is slightly above values reported for pure $LiBH_4$ (2.2 V *vs.* Li^+/Li).[15,50] The obtained result suggests that the addition of ZrO_2 slightly affects the electrochemical stability window of $LiBH_4$, and it can cause side reactions during galvanostatic cycling, influencing the performance of the system. On the contrary, the addition of MgO, as reported in literature[25] did not affect the electrochemical stability window, which remained in line with the values of pure $LiBH_4$.[29,32]

Battery cycling

The electrochemical performances of **RC 5** as SSE were evaluated in a SSB, using TiS_2 as the positive electrode and lithium metal as the negative electrode. Lithium was chosen for its higher energy density compared to commercial graphitic anodes,[51] while TiS_2 is a common choice for $LiBH_4$-based SSBs.[25,52] Two different profiles (*i.e.* CC and PC) were followed for battery cycling. The use of a PC profile follows the approach of Reisecker *et al.*, who reported that applying current pulses with short durations can extend the stability range of a SSE and can reduce the growth rate of lithium dendrites.[53]

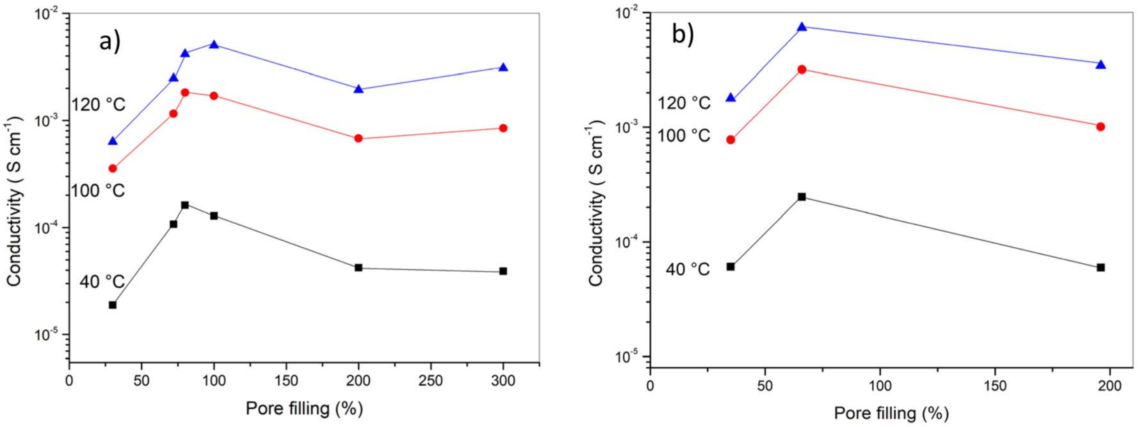

Fig. 5 Li-ion conductivity at 40 °C, 100 °C and 120 °C reported as a function of pore filling, with lines as a guide for the eyes, for (a) samples from **RC 1** to **RC 6** and for (b) samples from **OX 1** to **OX 3**.

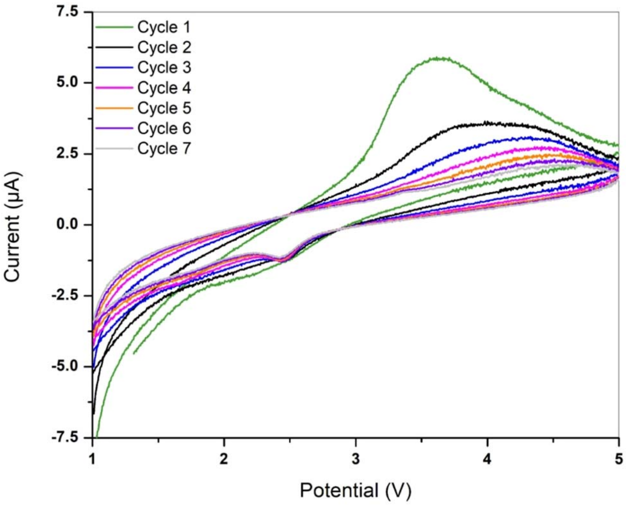

Fig. 6 Linear sweep voltammograms of cycle from 1 to 7 with Li|S-SE|**RC 5**: CB|stainless steel cell at scan rates of 100 μV s^{-1} from 1 to 5 V *vs.* Li+/Li at RT.

The specific discharge capacity was obtained by dividing the delivered capacity of the battery cell per gram of active cathode material, and results are shown in Fig. 7a. It is worth noting that, applying both a CC and a PC profiles, the first two cycles have a lower specific discharge capacity, if compared to the following cycles, suggesting the formation of the solid electrolyte interface (SEI) during these initial cycles. Unemoto *et al.*[52] already reported a similar phenomenon for a LiBH4-based SSB. The battery tested with a CC profile experienced a short circuit after only six charge/discharge cycles, likely due to the formation and propagation of dendrites. In contrast, the battery tested under a PC profile managed to cycle up to 16 times. After that, the experiment was stopped, as the battery capacity had dropped below 20% of its original capacity, even though no short circuits were observed. The highest specific capacity, obtained during the third discharge for the CC profile, was equal to 113.4 mA h g^{-1}, while for the PC profile, it was 75.4 mA h g^{-1}.

Overall, the use of a CC profile allowed to retain a higher capacity compared to the use of a PC profile, as shown in Fig. 7a. This difference could be attributed to two main factors. First, despite being prepared in the same way, the two tested batteries might not be perfectly identical, due to variations introduced during assembly by the operator. Second, during the PC profile, as shown in Fig. S12 and S13 in the ESI,† the upper charge limit of 2.5 V was not consistently reached in each cycle, whereas during the CC profile, it was always reached after the initial SEI formation. This was due to the exit conditions for the PC charge profile, so that, in some cases, the charge was interrupted by reaching the maximum time defined for the process.

Fig. 7b presents the discharge capacity retention of the batteries, tested under both CC and PC profiles. Normalization was achieved by excluding the first two SEI formation cycles and designating the specific capacity of cycle 3 as the 100% reference. Under both CC and PC profiles, the specific capacity declines sharply after the first cycle (4th considering the entire cycle life). The preservation of specific capacity was not observed using the PC profile, resulting in a 46% drop from the initial capacity by six cycles.

The energy throughput was calculated by integrating the power in absolute value *vs.* time peaks, and it turned out equal to 0.0414 W h and 0.0618 W h, for batteries tested under CC and the PC profiles, respectively. The higher energy throughput value obtained using the PC profile was expected, since the battery was able to retain its specific capacity for a longer number of cycles.

Overall, the performance of the SSB based on the $LiBH_4$–MgO system, which was able to cycle up to 65 times with a discharge capacity retention of more than 80% at 60 °C,[25] is better than that observed for the $LiBH_4$–ZrO_2 system. In order to explain this difference, the Li-ion conductivity of the SSE selected for both batteries are compared in Fig. S14,† and properties for selected SSEs and for pure oxides are reported in Table S4 in the ESI.† It is evident that the SSE used for the $LiBH_4$–MgO SSB shows a higher Li-ion conductivity at RT, with respect to that of the SSE used for the $LiBH_4$–ZrO_2 SSB. In

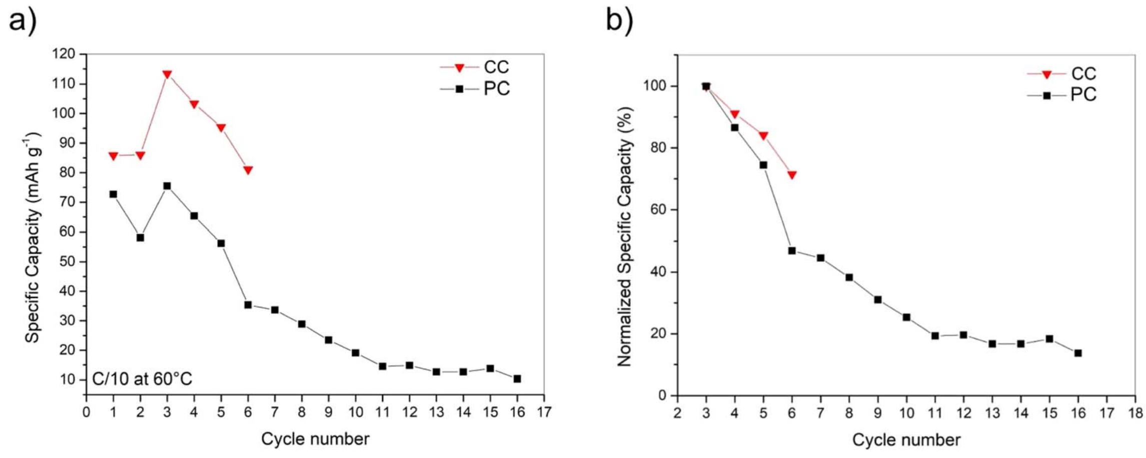

Fig. 7 Specific discharge capacity (a) and discharge capacity retention (b) of the SSB under CC and PC profiles. The value obtained for the third cycle was taken as 100% of the battery capacity.

addition, the activation energy for Li-ion conduction is much lower for the $LiBH_4$–MgO SSE with respect to that of $LiBH_4$–ZrO_2 SSE. On the other hand, both samples have a 100% of pore filling, but the estimated thickness of the $LiBH_4$ layer is more than double in the $LiBH_4$–ZrO_2 SSE with respect to that of the $LiBH_4$–MgO SSE. This is basically due the difference on the surface area of the oxides used to prepare the composites. It is also evident that ZrO_2 has a higher enthalpy of formation with respect to MgO, suggesting a stronger stability of the oxide with respect to possible reactions with $LiBH_4$. As a consequence, the formation of a highly conductive layer at the $LiBH_4$-oxide interface is easier for the $LiBH_4$–MgO composite than for the $LiBH_4$–ZrO_2 one. So, observed differences in the performance of the compared batteries could be possible due to the different nature of the oxides and thickness of bulk $LiBH_4$ layer. In addition, an oxide with a higher BET surface area and a thinner layer of $LiBH_4$, as in the case of MgO SSE, likely allows the formation of a better SEI between the anode and the cathode of the SSB. Further investigations are required to understand the potential effects of different pore filling ratios.

Conclusions

In this study, SSEs based on the $LiBH_4$–ZrO_2 system were investigated. Composite samples were synthesized *via* ball milling, using ZrO_2 with different specific surface areas and considering various $LiBH_4/ZrO_2$ ratios. XRD analysis highlighted the formation of a new phase at the interface between $LiBH_4$ and ZrO_2, which was not detected by IR-ATR spectroscopy. The highest Li-ion conductivity achieved at 40 °C was 2.45×10^{-4} S cm^{-1}, approximately four orders of magnitude higher than that of pure $LiBH_4$. The conductivity of the composites was found to be related to the volume fraction of $LiBH_4$, which governs the filling of ZrO_2 pore volume. Furthermore, the activation energy (E_a) values obtained were significantly lower than those reported in the literature for pure $LiBH_4$. The formation of a highly conductive interfacial layer influenced the electrochemical stability window, resulting in an oxidative stability limit of approximately 2.4 V *vs.* Li^+/Li, slightly higher than that of pure $LiBH_4$ (2.2 V *vs.* Li^+/Li). Battery tests performed at 60 °C suggested the formation of a stable solid electrolyte interphase during the first two charge/discharge cycles, under both constant current and pulse current profiles. Under the CC profile, the battery operated for four cycles with an initial specific capacity of 113.4 mA h g^{-1}, whereas under the PC profile, it operated for 14 cycles with an initial specific capacity of 75.4 mA h g^{-1}. In both cases, a rapid decrease in specific capacity was observed, with values dropping below 80% of the initial capacity within the first three cycles. In conclusion, the study demonstrates the feasibility of assembling a solid-state battery (SSB) using a $LiBH_4$–ZrO_2based SSE. However, the battery performance remains suboptimal, and the results should be considered as a proof of concept. Further investigations into the origin of capacity fading, particularly under pulse charging conditions, are necessary to improve battery durability.

Data availability

The data supporting this article have been included as part of the ESI†.

Author contributions

Conceptualization: Ngene, De Jongh, Sgroi, Baricco; methodology: Gulino, Sgroi; formal analysis and investigation: Mazzucco, Wolterbeek, Gulino, Sgroi; writing – original draft preparation: Mazzucco, Gulino; writing – review and editing: Mazzucco, Gulino, Sgroi, Ngene, De Jongh, Baricco; funding acquisition: De Jongh, Baricco; resources: Ngene, De Jongh, Baricco; supervision: Ngene, De Jongh, Baricco.

Conflicts of interest

All authors declare that they have no conflicts of interest.

Acknowledgements

Support from the Project CH4.0 under the MUR program “Dipartimenti di Eccellenza 2023–2027” (CUP: D13C22003520001) is acknowledged. Peter Ngene and Petra E. de Jongh acknowledge financial support from the Dutch Research Council (NWO) *via* the BatteryNL project (NWA.1389.20.089) of the NWA-ORC programme.

References

1 Y. Pang, Y. Liu, J. Yang, S. Zheng and C. Wang, Hydrides for solid-state batteries: A review, *Mater. Today Nano*, 2022, **18**, 100194, DOI: **10.1016/J.MTNANO.2022.100194**.

2 J. C. Bachman, S. Muy, A. Grimaud, H.-H. Chang, N. Pour, S. F. Lux, O. Paschos, F. Maglia, S. Lupart, P. Lamp, L. Giordano and Y. Shao-Horn, Inorganic Solid-State Electrolytes for Lithium Batteries: Mechanisms and Properties Governing Ion Conduction, *Chem. Rev.*, 2016, **116**, 140–162, DOI: **10.1021/acs.chemrev.5b00563**.

3 K. Xu, Nonaqueous liquid electrolytes for lithium-based rechargeable batteries, *Chem. Rev.*, 2004, **104**, 4303–4417, DOI: **10.1021/cr030203g**.

4 X. Feng, M. Ouyang, X. Liu, L. Lu, Y. Xia and X. He, Thermal runaway mechanism of lithium ion battery for electric vehicles: A review, *Energy Storage Mater.*, 2018, **10**, 246–267, DOI: **10.1016/J.ENSM.2017.05.013**.

5 R. Chen, W. Qu, X. Guo, L. Li and F. Wu, The pursuit of solid-state electrolytes for lithium batteries: from comprehensive insight to emerging horizons, *Mater. Horiz.*, 2016, **3**, 487, DOI: **10.1039/c6mh00218h**.

6 A. Ahniyaz, I. de Meatza, A. Kvasha, O. Garcia-Calvo, I. Ahmed, M. F. Sgroi, M. Giuliano, M. Dotoli, M. A. Dumitrescu, M. Jahn and N. Zhang, Progress in solid-state high voltage lithium-ion battery electrolytes, *Adv. Appl. Energy*, 2021, **4**, 100070, DOI: **10.1016/J.ADAPEN.2021.100070**.

7 M. Murayama, R. Kanno, M. Irie, S. Ito, T. Hata, N. Sonoyama and Y. Kawamoto, Synthesis of New Lithium Ionic Conductor Thio-LISICON—Lithium Silicon Sulfides System, *J. Solid State Chem.*, 2002, **168**, 140–148, DOI: 10.1006/JSSC.2002.9701.

8 S. Stramare, V. Thangadurai and W. Weppner, Lithium Lanthanum Titanates: A Review, *Chem. Mater.*, 2003, **15**, 3974–3990, DOI: 10.1021/cm0300516.

9 B. A. Boukamp and R. A. Huggins, Ionic conductivity in lithium imide, *Phys. Lett. A*, 1979, **72**, 464–466, DOI: 10.1016/0375-9601(79)90846-6.

10 M. Matsuo and S. I. Orimo, Lithium Fast-Ionic Conduction in Complex Hydrides: Review and Prospects, *Adv. Energy Mater.*, 2011, **1**, 161–172, DOI: 10.1002/AENM.201000012.

11 H. Oguchi, M. Matsuo, T. Sato, H. Takamura, H. Maekawa, H. Kuwano and S. Orimo, Lithium-ion conduction in complex hydrides LiAlH4 and Li 3 AlH6, *J. Appl. Phys.*, 2010, **107**(9), 6104, DOI: 10.1063/1.3356981/369822.

12 Y. Nakagawa, T. Kimura, S. Isobe and T. Shibayama, Effects of Defective Boron Nitride Additives on Lithium-Ion Conductivity and Hydrogen-Desorption Properties of LiAlH4, *J. Phys. Chem. C*, 2020, **124**, 10398–10407, DOI: 10.1021/acs.jpcc.0c02312.

13 S. Kim, N. Toyama, H. Oguchi, T. Sato, S. Takagi, T. Ikeshoji and S. I. Orimo, Fast Lithium-Ion Conduction in Atom-Deficient closo-Type Complex Hydride Solid Electrolytes, *Chem. Mater.*, 2018, **30**, 386–391, DOI: 10.1021/acs.chemmater.7b03986.

14 W. S. Tang, A. Unemoto, W. Zhou, V. Stavila, M. Matsuo, H. Wu, S. I. Orimo and T. J. Udovic, Unparalleled lithium and sodium superionic conduction in solid electrolytes with large monovalent cage-like anions, *Energy Environ. Sci.*, 2015, **8**, 3637–3645, DOI: 10.1039/C5EE02941D.

15 V. Gulino, M. Brighi, E. M. Dematteis, F. Murgia, C. Nervi, R. Černý and M. Baricco, Phase Stability and Fast Ion Conductivity in the Hexagonal LiBH4–LiBr–LiCl Solid Solution, *Chem. Mater.*, 2019, **31**, 5133–5144, DOI: 10.1021/acs.chemmater.9b01035.

16 R. Miyazaki, T. Karahashi, N. Kumatani, Y. Noda, M. Ando, H. Takamura, M. Matsuo, S. Orimo and H. Maekawa, Room temperature lithium fast-ion conduction and phase relationship of LiI stabilized LiBH4, *Solid State Ionics*, 2011, **192**, 143–147, DOI: 10.1016/J.SSI.2010.05.017.

17 M. Matsuo, Y. Nakamori, S. I. Orimo, H. Maekawa and H. Takamura, Lithium superionic conduction in lithium borohydride accompanied by structural transition, *Appl. Phys. Lett.*, 2007, **91**, 224103, DOI: 10.1063/1.2817934/334551.

18 L. H. Rude, E. Groppo, L. M. Arnbjerg, D. B. Ravnsbæk, R. A. Malmkjær, Y. Filinchuk, M. Baricco, F. Besenbacher and T. R. Jensen, Iodide substitution in lithium borohydride, LiBH4-LiI, *J. Alloys Compd.*, 2011, **509**, 8299–8305, DOI: 10.1016/J.JALLCOM.2011.05.031.

19 A. Mazzucco, E. M. Dematteis, V. Gulino, M. Corno, M. F. Sgroi, M. Palumbo and M. Baricco, Experimental and theoretical studies of the LiBH4–LiI phase diagram, *RSC Adv.*, 2024, **14**, 12038–12048, DOI: 10.1039/D4RA01642D.

20 V. Gulino, L. Barberis, P. Ngene, M. Baricco and P. E. De Jongh, Enhancing Li-Ion Conductivity in LiBH4-Based Solid Electrolytes by Adding Various Nanosized Oxides, *ACS Appl. Energy Mater.*, 2020, **3**, 4941–4948, DOI: 10.1021/acsaem.9b02268.

21 Y. S. Choi, Y. S. Lee, K. H. Oh and Y. W. Cho, Interface-enhanced Li ion conduction in a LiBH4–SiO2 solid electrolyte, *Phys. Chem. Chem. Phys.*, 2016, **18**, 22540–22547, DOI: 10.1039/C6CP03563A.

22 Y. S. Choi, Y. S. Lee, D. J. Choi, K. H. Chae, K. H. Oh and Y. W. Cho, Enhanced Li Ion Conductivity in LiBH4-Al2O3 Mixture via Interface Engineering, *J. Phys. Chem. C*, 2017, **121**, 26209–26215, DOI: 10.1021/acs.jpcc.7b08862.

23 H. Mizuochi, Y. Nakagawa, T. Shibayama, Y. Yao, F. Guo, H. Miyaoka and T. Ichikawa, Effects of Oxide Morphology on Lithium-Ion Conductivity of LiBH4-Al2O3 Composites, *ACS Appl. Energy Mater.*, 2025, **8**(1), 518–528, DOI: 10.1021/acsaem.4c02653.

24 S. Zeng, K. Ren, H. Ding, S. Xu, H. W. Li and Y. Li, Stabilization of fast lithium-ionic conduction phase of nanaoconfined LiBH4 for lithium metal solid-state batteries, *Chem. Commun.*, 2025, **61**, 929–932, DOI: 10.1039/D4CC05329J.

25 V. Gulino, M. Brighi, F. Murgia, P. Ngene, P. De Jongh, R. Černý and M. Baricco, Room-Temperature Solid-State Lithium-Ion Battery Using a LiBH 4-MgO Composite Electrolyte, *ACS Appl. Energy Mater.*, 2021, **4**, 1228–1236, DOI: 10.1021/ACSAEM.0C02525.

26 Y. Wei, Z. Li, Z. Chen, P. Gao, M. Gao, C. Yan, Z. Wu, Q. Ma, Y. Jiang, X. Yu, X. Zhang, Y. Liu, Y. Yang, M. Gao, W. Sun, Z. Qu, J. Chen and H. Pan, A wide temperature 10 V solid-state electrolyte with a critical current density of over 20 mA cm 2, *Energy Environ. Sci.*, 2023, **16**, 4679, DOI: 10.1039/d3ee02301j.

27 Y. Huang, Y. Zheng, J. Li, X. Bao, J. Guo, J. Shen, Y. Guo, Q. Zhang, J. Li, W. Lei and H. Shao, Li- and Mg-based borohydrides for hydrogen storage and ionic conductor, *J. Mater. Sci. Technol.*, 2023, **153**, 181–204, DOI: 10.1016/J.JMST.2022.12.058.

28 Y. Sakamoto, A. Ishii, T. Shiratori, I. Oikawa and H. Takamura, Sintering-free preparation of Li7La3Zr2O12–LiBH4-based solid-state electrolytes and their electrical conductivities, *Electrochim. Acta*, 2023, **457**, 142488, DOI: 10.1016/J.ELECTACTA.2023.142488.

29 S. F. H. Lambregts, E. R. H. Van Eck, P. Ngene and A. P. M. Kentgens, The Nature of Interface Interactions Leading to High Ionic Conductivity in LiBH4/SiO2Nanocomposites, *ACS Appl. Energy Mater.*, 2022, **5**, 8057–8066, DOI: 10.1021/acsaem.2c00527.

30 S. F. H. Lambregts, E. R. H. Van Eck, S. Suwarno, P. Ngene, P. E. De Jongh and A. P. M. Kentgens, Phase Behavior and Ion Dynamics of Nanoconfined LiBH4 in Silica, *J. Phys. Chem. C*, 2019, **123**, 25559–25569, DOI: 10.1021/acs.jpcc.9b06477.

31 L. M. De Kort, M. Lazemi, A. Longo, V. Gulino, H. P. Rodenburg, D. Blanchard, C. Sahle, M. Sundermann, H. Gretarsson, A. M. J. Van Der Eerden, H. Elnaggar,

F. M. F. De Groot and P. Ngene, Deciphering the Origin of Interface-Induced High Li and Na Ion Conductivity in Nanocomposite Solid Electrolytes Using X-Ray Raman Spectroscopy, *Adv. Energy Mater.*, 2024, 2303381, DOI: **10.1002/AENM.202303381**.

32 Y. Nakagawa, T. Sendo and T. Shibayama, Enhanced Li-ion conductivity in LiBH4–ZrO2 nanocomposites and nanoscale Li imaging by energy-filtered transmission electron microscopy, *Chem. Commun.*, 2023, **59**, 10912–10915, DOI: **10.1039/D3CC02860G**.

33 T. Scheiber, B. Gadermaier, K. Hogrefe, R. Zettl, H. Martin and R. Wilkening, Thermoresistant Defects Preserve Fast Ion Conduction in LiBH4–ZrO2 Conductor–Insulator Nanocomposites, *Chem. Mater.*, 2023, **35**(24), 10504–10514, DOI: **10.1021/ACS.CHEMMATER.3C02026**.

34 S. Brunauer, P. H. Emmett and E. Teller, Adsorption of Gases in Multimolecular Layers, *J. Am. Chem. Soc.*, 1938, **60**, 309–319, DOI: **10.1021/ja01269a0233**.

35 V. Dimitrov and S. Sakka, Electronic oxide polarizability and optical basicity of simple oxides. I, *J. Appl. Phys.*, 1996, **79**, 1736–1740, DOI: **10.1063/1.360962**.

36 L. . Lutterotti, M. S. Matthies and W. H. R. Wenk, MAUD: A Friendly Java Program for Material Analysis Using Diffraction, *Mater. Anal. Using Diffr.*, 1999, 14–15.

37 H. P. Rodenburg and P. Ngene, DECiM: Determination of equivalent circuit models, *SoftwareX*, 2024, **27**, 101807, DOI: **10.1016/J.SOFTX.2024.101807**.

38 H. Hagemann, Y. Filinchuk, D. Chernyshov and W. Van Beek, Lattice anharmonicity and structural evolution of LiBH4: an insight from Raman and X-ray diffraction experiments, *Phase Transitions*, 2009, **82**, 344–355, DOI: **10.1080/01411590802707688**.

39 O. Zavorotynska, M. Corno, E. Pinatel, L. H. Rude, P. Ugliengo, T. R. Jensen and M. Baricco, Theoretical and Experimental Study of LiBH4-LiCl Solid Solution, *Crystals*, 2012, **2**(2), 144–158, DOI: **10.3390/CRYST2010144**.

40 L. H. Rude, O. Zavorotynska, L. M. Arnbjerg, D. B. Ravnsbæk, R. A. Malmkjær, H. Grove, B. C. Hauback, M. Baricco, Y. Filinchuk, F. Besenbacher and T. R. Jensen, Bromide substitution in lithium borohydride, LiBH4–LiBr, *Int. J. Hydrogen Energy*, 2011, **36**, 15664–15672, DOI: **10.1016/J.IJHYDENE.2011.08.087**.

41 J. C. Valmalette and M. Isa, Size effects on the stabilization of ultrafine zirconia nanoparticles, *Chem. Mater.*, 2002, **14**, 5098–5102, DOI: **10.1021/cm021233n**.

42 M. Asiltürk, E. Burunkaya, F. Sayilkan, N. Kiraz and E. Arpaç, Structural and optical properties of thin films prepared from surface modified ZrO2, *J. Non-Cryst. Solids*, 2011, **357**, 206–210, DOI: **10.1016/J.JNONCRYSOL.2010.09.034**.

43 V. Gulino, A. Wolczyk, A. A. Golov, R. A. Eremin, M. Palumbo, C. Nervi, V. A. Blatov, D. M. Proserpio and M. Baricco, Combined DFT and geometrical–topological analysis of Li-ion conductivity in complex hydrides, *Inorg. Chem. Front.*, 2020, **7**, 3115–3125, DOI: **10.1039/D0QI00577K**.

44 W. Zhao, J. Yi, P. He and H. Zhou, Solid-State Electrolytes for Lithium-Ion Batteries: Fundamentals, Challenges and Perspectives, *Electrochem. Energy Rev.*, 2019, **2**(4), 574–605, DOI: **10.1007/S41918-019-00048-0**.

45 A. Sakuda, A. Hayashi and M. Tatsumisago, Sulfide Solid Electrolyte with Favorable Mechanical Property for All-Solid-State Lithium Battery, *Sci. Rep.*, 2013, **3**(1), 1–5, DOI: **10.1038/srep02261**.

46 J. M. Doux, Y. Yang, D. H. S. Tan, H. Nguyen, E. A. Wu, X. Wang, A. Banerjee and Y. S. Meng, Pressure effects on sulfide electrolytes for all solid-state batteries, *J. Mater. Chem. A*, 2020, **8**, 5049–5055, DOI: **10.1039/C9TA12889A**.

47 L. Lamiri and B. Nessark, Electrochemical behavior, characterization and corrosion protection properties of poly(bithiophene+2-methylfuran) copolymer coatings on A304 stainless steel, *E-Polym.*, 2018, **18**, 143–151, DOI: **10.1515/epoly-2017-0057**.

48 P. Zhu, D. Gastol, J. Marshall, R. Sommerville, V. Goodship and E. Kendrick, A review of current collectors for lithium-ion batteries, *J. Power Sources*, 2021, **485**, 229321, DOI: **10.1016/J.JPOWSOUR.2020.229321**.

49 M. A. Deyab and S. T. Keera, Cyclic voltammetric studies of carbon steel corrosion in chloride-formation water solution and effect of some inorganic salts, *Egypt. J. Pet.*, 2012, **21**, 31–36, DOI: **10.1016/J.EJPE.2012.02.005**.

50 R. Asakura, L. Duchêne, R. S. Kühnel, A. Remhof, H. Hagemann and C. Battaglia, Electrochemical Oxidative Stability of Hydroborate-Based Solid-State Electrolytes, *ACS Appl. Energy Mater.*, 2019, **2**, 6924–6930, DOI: **10.1021/acsaem.9b01487**.

51 J. B. Goodenough and P. Singh, Review—Solid Electrolytes in Rechargeable Electrochemical Cells, *J. Electrochem. Soc.*, 2015, **162**, A2387–A2392, DOI: **10.1149/2.0021514JES/XML**.

52 A. Unemoto, T. Ikeshoji, S. Yasaku, M. Matsuo, V. Stavila, T. J. Udovic and S. I. Orimo, Stable Interface Formation between TiS2 and LiBH4 in Bulk-Type All-Solid-State Lithium Batteries, *Chem. Mater.*, 2015, **27**, 5407–5416, DOI: **10.1021/acs.chemmater.5b02110**.

53 V. Reisecker, F. Flatscher, L. Porz, C. Fincher, J. Todt, I. Hanghofer, V. Hennige, M. Linares-Moreau, P. Falcaro, S. Ganschow, S. Wenner, Y. M. Chiang, J. Keckes, J. Fleig and D. Rettenwander, Effect of pulse-current-based protocols on the lithium dendrite formation and evolution in all-solid-state batteries, *Nat. Commun.*, 2023, **14**(1), 1–12, DOI: **10.1038/s41467-023-37476-y**.